Polymer Testing 146 (2025) 108794

Contents lists available at ScienceDirect

Polymer Testing

journal homepage: www.elsevier.com/locate/polytest

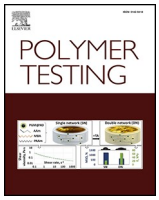

Layer-level constitutive material model for representing non-linear stress-strain relationships in continuous carbon fiber-reinforced 3D-printed composites

Csenge Tóth [a,b,*], Blanka Ilinyi [a], László Kovács [a]

[a] Department of Polymer Engineering, Faculty of Mechanical Engineering, Budapest University of Technology and Economics, Műegyetem rkp. 3, H-1111, Budapest, Hungary
[b] MTA-BME Lendület Lightweight Polymer Composites Research Group, Műegyetem rkp. 3, H-1111, Budapest, Hungary

A B S T R A C T

3D-printed thermoplastic composites reinforced with continuous fibers exhibit nonlinear mechanical responses mostly due to the viscoelastic matrix and the presence of voids. We present a layer-level constitutive material modeling framework to address this behavior. Unidirectional and multidirectional composites were prepared using Composite Filament Co-extrusion technology, then, the engineering constants required to describe the transversely isotropic materials were determined with tensile tests. We chose carbon fiber reinforcement and polyamide matrix, and the fiber volume fraction was 9.5–13.6 %. We used the Bogetti relationship based on the explicit Ramberg-Osgood equation to describe the stress-strain curves above the yield criterion. We applied the Hill model to rescale the principal stress-strain curves to the shear curve with good accuracy. 4-point bending simulations were prepared to evaluate the application boundaries, which showed that the model is applicable for thinner plate-like structures (with a thickness limit of 3 mm). Lastly, microtomography was employed to analyze the microstructure, quantify void content, and identify 3D-printing defects. A significant void content was found in the multidirectional specimens (19 %), which may account for the scatter in the test results and modeling discrepancies. Overall, we demonstrate the suitability of the proposed modeling method for describing nonlinear behavior, and it contributes to more accurate finite element models for 3D-printed thermoplastic composites.

1. Introduction

Continuous fiber-reinforced 3D-printed composites are becoming more popular in engineering applications. Application areas include aerospace and automotive, where lightweight, high-strength components are advantageous [1–3]; and robotics and automation, where high levels of customisability and potential added functional features are beneficial [4–6]. However, for 3D-printed composites to be suitable as load-bearing components, the predictability of their mechanical response and failure are key.

The mechanical characterization of 3D-printed continuous fiber-reinforced composites is complex due to their inhomogeneous and anisotropic nature. Inhomogeneities arise from manufacturing defects and the composite's multi-component structure [7,8]. Anisotropy results from the directional alignment of fibers, which enhances mechanical properties along the fiber direction [9]. With micromechanical models, a mechanically homogeneous layer is modeled by considering the constituent ratios and their engineering constants. Using mixing rules, the material properties of a layer can be calculated based on the mechanical characteristics of the fibers, the matrix, and the fiber volume fraction. Then, macromechanical models (often plate theories) are used to describe the laminate based on the properties of the homogeneous layers, and the layer order [10].

In the case of 3D-printed thermoplastic composites reinforced with continuous fibers, the nonlinear mechanical response may arise due to several factors. The thermoplastic matrix exhibits nonlinear behavior under large deformations due to viscoelasticity [11]. Interactions between the fibers and the matrix, including delamination, slip, and uneven stress distribution, further increase the nonlinearity by disrupting the effective load transfer. Different approaches have been used to address the nonlinearity of orthotropic material properties as a function of load. Chen and Sun [12] proposed a three-parameter plastic potential to describe the plastic behavior of Kevlar-aluminium composites, following the preliminary results of Kenaga et al. [13]. Later, Sun and Chen [14] developed this work further, where the nonlinear orthotropic material properties were derived on a micromechanical basis. They postulated fully linear elastic material properties for the fiber and isotropic ductile material behavior for the matrix material according to

* Corresponding author. Department of Polymer Engineering, Faculty of Mechanical Engineering, Budapest University of Technology and Economics, Műegyetem rkp. 3., H-1111, Budapest, Hungary.
E-mail address: tothcs@pt.bme.hu (C. Tóth).

https://doi.org/10.1016/j.polymertesting.2025.108794
Received 12 February 2025; Received in revised form 18 March 2025; Accepted 3 April 2025
Available online 3 April 2025

the Mises flow law [15]. The obtained relations were finally verified by mechanical tests on oriented unidirectional (UD) specimens.

However, in the case of 3D-printed composites, fewer methods can be found to address nonlinearity. I. M. Alarifi [16] presented a finite element analysis for short carbon-fiber reinforced polyethylene terephthalate glycol (PETG) composites. A quasi-isotropic, linear elastic material was assumed, and a nonlinear geometry was used to calculate stress and strain. The finite element (FE) model provided an approximation for yield strength, strain at failure, and elastic modulus, with the largest relative errors of 32 %, 20 %, and 29 %, respectively. Generally, the model curves followed well the experimental curves until the yield point, but the deviation increased at the hardening phase. Hou et al. [17] presented a constitutive model for continuous aramid fiber-reinforced poly (lactic acid) (PLA) composites. The material properties were determined experimentally, and the Classical Laminate Theory with Hashin failure criterion was applied. The modeled stress-strain curve did not follow well the nonlinear response shown on the measurement curve. Avanzini et al. [18] presented an embedded elements approach for carbon fiber-reinforced polyamide (PA) composites. The fibers and the matrix were assigned material properties and assembled. Unlike homogenization methods, equivalent layer properties were not calculated, but the lamina properties were defined using the embedded fiber and matrix elements. The model predicted the elastic moduli with a maximum of 3.6 % error, however, it can only be used for the initial stress-strain phase as non-linear materials were not considered. Seifans et al. [19] presented an elastic/viscoplastic model to predict the creep behavior of carbon fiber-reinforced PA composites. In the model, an orthotropic and homogeneous material is assumed. The authors found that 3D-printed composites are more prone to deformation than conventional thermoplastic composites, probably due to the higher amount of defects they contain. Polyzos et al. [20] presented a numerical three-step multi-scale model for continuous fiber-reinforced PA composites. At the micro-scale, the concentric cylinder micromechanical model was developed and the Representative Volume Element (RVE) concept was implemented to predict the elastic properties. At the meso-scale level, the authors applied different void models to account for the porosity. Lastly, different fiber orientations and layer orders were analyzed at the macro-scale. The authors highlighted that the porosity and the unique and often weak interfacial properties of 3D-printed composites require special modeling methods. Gao et al. [21] developed a progressive failure finite analysis model for continuous carbon fiber-reinforced PA composites. The RVE was defined based on micrographs, then the Chamis model was used for tensile strength prediction. Failure was predicted with a three-dimensional Hashin criterion. Overall, the method was proven useful in the case of linear response.

In this paper, we present a layer-level constitutive material model for modeling the non-linear mechanical response of continuous fiber-reinforced 3D-printed composites. Literature shows that current methods do not characterize adequately the stress-strain relationship above the yield point, due to the viscoplastic nature of the thermoplastic matrix and the porosity of the composites. We present a novel simulation process with the combination of the Hill yield criterion and the Bogetti equation, which is suitable for the modeling of nonlinear behavior. The method contributes to more reliable simulation predictions for 3D-printed composites.

2. Computational simulations

2.1. Linear characteristics

Plate theories provide a link between the layer-level mechanical model and the laminate-level behavior. Kirchhoff plate theory, or classical laminate theory (CLT), can be applied to thin plates with small deformations [10,22]. In the method, the laminate thickness is neglected and considered as a composite shell, thus the plate is only considered in a plane stress state. The basic assumption of plate theory is that the plate

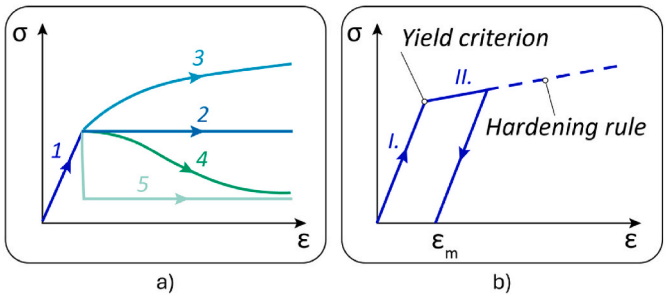

Fig. 1. a) Main types of elastoplastic models: 2) ideally plastic, 3) nonlinear hardening, 4) nonlinear softening, 5) brittle softening; b) Parts of a bilinear elastoplastic model.

can only deform with strains interpreted in the midplane and along the curvature of the midplane. The layers do not move relative to each other, so there is no interlayer deformation. In this case, the value of the interlayer stiffness is infinitely large, and therefore no interlayer shear stress occurs. When applying the CLT theory, linear characteristics are assumed which means that the stiffness matrix of each layer operates with constant moduli, assuming a linear relationship between elongation/curvature and the corresponding force/moment in the deformed state. Thus, the deformation vector can be given by the midplane elongation and the curvature, taking into account deformations due to thermal expansion.

The FE models were built in ANSYS Workbench 2021 R2, Mechanical in combination with the Ansys Composite PrePost (ACP) module for automated composite layup build. In the computations, first, the submatrices [A], [B], and [D] are constructed for each finite element, and then the stiffness matrix of the complete finite element model system is constructed. In the third step, the software iterates the deformed shape giving the energy minimum, and then gives the layer-level specific strains. Finally, the specific strains are used to calculate the values of the layer stresses using the orthotropic Hooke's law (Eq. (1)). We have used shell elements in which only in-plane stress states are assumed. We characterized the materials by the four engineering constants: E_{11}, E_{22}, G_{12}, and ν_{12}.

$$\begin{bmatrix} \varepsilon_{11} \\ \varepsilon_{22} \\ \varepsilon_{33} \\ \gamma_{23} \\ \gamma_{13} \\ \gamma_{12} \end{bmatrix} = \begin{bmatrix} \frac{1}{E_{11}} & \frac{-\nu_{21}}{E_{22}} & \frac{-\nu_{31}}{E_{33}} & 0 & 0 & 0 \\ \frac{-\nu_{12}}{E_{11}} & \frac{1}{E_{22}} & \frac{-\nu_{32}}{E_{33}} & 0 & 0 & 0 \\ \frac{-\nu_{13}}{E_{11}} & \frac{-\nu_{23}}{E_{22}} & \frac{1}{E_{33}} & 0 & 0 & 0 \\ 0 & 0 & 0 & \frac{1}{G_{23}} & 0 & 0 \\ 0 & 0 & 0 & 0 & \frac{1}{G_{13}} & 0 \\ 0 & 0 & 0 & 0 & 0 & \frac{1}{G_{12}} \end{bmatrix} \cdot \begin{bmatrix} \sigma_{11} \\ \sigma_{22} \\ \sigma_{33} \\ \tau_{23} \\ \tau_{13} \\ \tau_{12} \end{bmatrix} \quad (1)$$

where ε (−) is the normal strain in the principal direction, γ (−) is the shear strain, E (MPa) is the Young's modulus in the principal directions, ν (−) is the Poisson's ratios relating strain in one direction to stress in another, G (MPa) is the Shear modulus in the principal planes, σ (MPa) is the normal stress and τ (MPa) is the shear stress.

2.2. Nonlinear characteristics

In the linear orthotropic material model, the elements of the stiffness matrix correspond to the partial derivatives of the stress in a given direction with respect to the strain in the same direction [10]. Therefore, if the elements of the matrix Q are expressed in terms of material constants, it will be suitable for describing linear behavior only. If the

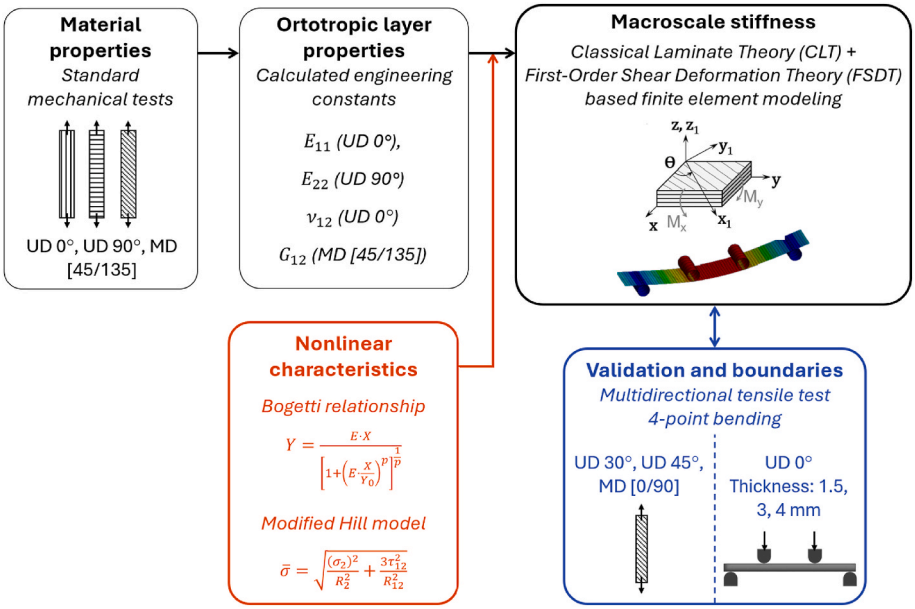

Fig. 2. Flowchart of the method presented in the paper.

behavior of the material under consideration at higher deformations is other than linear, the model will be inaccurate, as new moduli would have to be defined for each stress level. The material behavior of composites with thermoplastic matrix exhibits significant nonlinearity. In thermoplastic polymers, secondary chemical bonds form between the linear molecular chains, making them more easily separable. As a result, thermoplastic polymers experience permanent deformation even under lower stress levels. Additionally, they exhibit viscoelastic behavior, which contributes to their nonlinear characteristics. Fig. 1/a shows the main types of models describing elastoplastic behavior: ideally plastic, nonlinear hardening, nonlinear softening, and brittle softening [23,24]. Fig. 1/b shows the parts of a linear elastoplastic model. Once the yield point is crossed, plastic deformation starts immediately, i.e. the model behavior is time independent and the deformation is irreversible. The theory contains two essential elements, the yield criterion and the hardening rule.

To describe the nonlinear behavior, an elastoplastic model typically used for plastic deformation in materials was applied. Fig. 2 shows a flowchart of the method presented in this paper. This model defines a stress threshold corresponding to the yield point, beyond which plastic deformation begins. In this setting, plastic deformation initiates immediately after the yield point is surpassed, indicating that the model is time-independent with irreversible deformation. The theory includes two essential components: the yield criterion and the hardening rule. To describe the stress-strain curve in a given in-plane direction above the yield criterion, we used the Bogetti relationship (Eq. (2)) [25]:

$$Y = \frac{E \cdot X}{\left[1 + \left(E \cdot \frac{X}{Y_0}\right)^p\right]^{\frac{1}{p}}} \tag{2}$$

where Y (MPa) is the stress in fiber, transverse, or shear direction, X (−) is the strain and E, Y_0, and p are shape parameters describing the initial slope, the asymptote, and the curvature, respectively.

Then, we applied the Hill yield criterion (Eq. (3)) [26]. General nonlinear orthotropic material models are typically approximations implemented in a finite element solver. In ANSYS, Hill's orthotropic plastic law is available, which is typically used for thermoplastic matrix composites. By combining the linearly elastic orthotropic material model with the Hill plastic model, an orthotropic elastoplastic material model is created that accurately captures the measured nonlinear behavior in both the elastic and plastic regions.

$$f(\sigma) = \bar{\sigma} - \sigma_Y \tag{3}$$

where f (−) is the current value of the function defining the yield law, $\bar{\sigma}$ (MPa) is the equivalent of stress and σ_Y (MPa) is the current yield criterion. The value of f indicates the deformation stage of the curve. If f < 0, the curve is in the elastic deformation stage, and if f = 0, the material undergoes elastoplastic deformation (f should not take a positive value).

For nonlinear hardening behavior, the yield stress is a function of the equivalent plastic elongation, so the Hill criterion can be written according to Eq. (4):

$$f(\sigma) = \bar{\sigma} - \sigma_Y\left(\bar{\varepsilon}^p\right) \tag{4}$$

The equivalent stress in the Hill model is a generalization of von Mises theory for orthotropic materials, where the stress components in each direction are weighted by the R-ratios. R_1, R_2, and R_3, as well as R_{12}, R_{23}, and R_{13}, are indexed to the principal directions of the orthotropic materials.

When describing the behavior of continuous fiber-reinforced composites, to determine the individual R values we have to consider the geometric characteristics of the unidirectional (UD) layers and the mechanical properties arising from material inhomogeneity. For tensile stresses aligned with the fiber direction, the material exhibits linear behavior, so the model should be configured so that the stress value does not approach the theoretical yield stress. This is to ensure a linear response throughout the simulation. Therefore, we set the R_1 value for the fiber direction to a very high value (or infinity). The UD layers can be represented by transversely isotropic material models, so the ratio values of R_2 to R_3 and R_{12} to R_{13} remain consistent. From this, a modified version of the Hill yield criterion can be derived, accounting for nonlinear transverse stress and shear. The equivalent stress is given with Eq. (5), and the equivalent increase in strain is given with Eq. (6).

$$\bar{\sigma} = \sqrt{\frac{(\sigma_2)^2}{R_2^2} + \frac{3\tau_{12}^2}{R_{12}^2}} \tag{5}$$

$$d\bar{\varepsilon}^p = \sqrt{R_2^2 \cdot \left(d\varepsilon_2^p\right)^2 + \frac{R_{12}^2}{3} \cdot \left(d\gamma_{12}^p\right)^2} \tag{6}$$

Thus, stress deformation curves can be constructed (Eq. (7) and (8)),

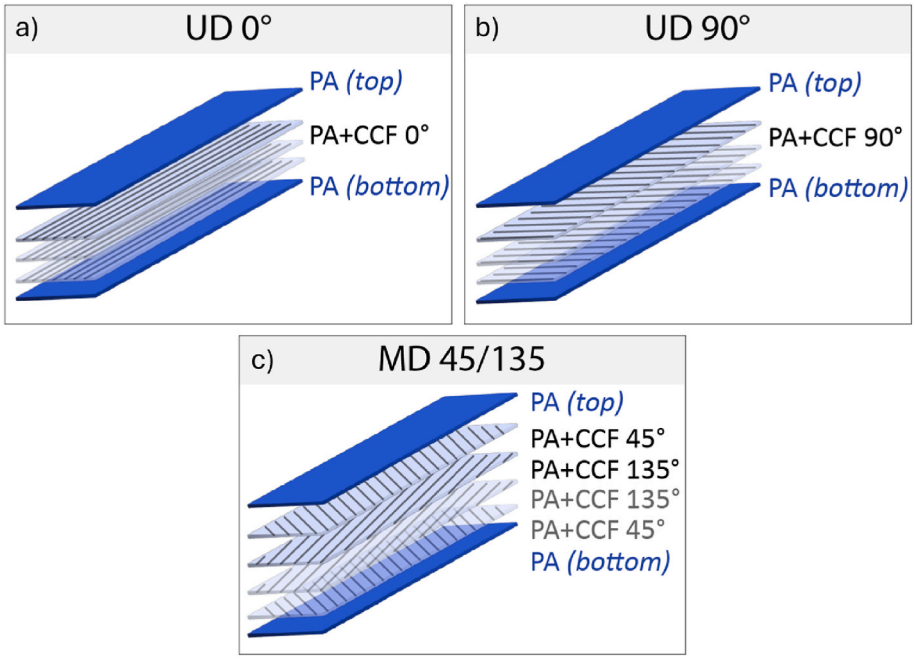

Fig. 3. Layer orders of the specimens a) UD 0°, b) UD 90°, c) MD 45°/135°. For the UD 30° and UD 45°, the fiber orientation is rotated with respect to 0° and the layering is the same as in a). For MD 0°/90°, the fiber orientation is rotated with respect to 0° and the layering is the same as in c).

taking into account that the total deformation component in a given ply-specific principal direction can be given as the sum of elastic and plastic deformations.

$$\varepsilon_i = \varepsilon_i^e + \varepsilon_i^p \tag{7}$$

$$\gamma_{ij} = \gamma_{ij}^e + \gamma_{ij}^p \tag{8}$$

where $\varepsilon_i^e, \gamma_{ij}^e$ (−) are the elastic deformations and $\varepsilon_i^p, \gamma_{ij}^p$ (−) are the plastic deformations.

The elastic deformations can be given with the engineering constants according to Hooke's law (Eq. (9) and (10)):

$$\varepsilon_{ii}^e = \frac{\sigma_{ii}}{E_i} - \nu_{ji}\frac{\sigma_{jj}}{E_j} - \nu_{kj}\frac{\sigma_{kk}}{E_k} \tag{9}$$

$$\gamma_{ij}^e = \frac{\tau_{ij}}{G_{ij}} \tag{10}$$

Using these relationships, the connection between total strain and the current stress state in the shear and transverse directions (where nonlinearity is assumed) can be derived. The R parameters are scaled relative to a reference yield curve, allowing the stress-strain relationship in the isolated direction to be determined by scaling in both directions using the equations above. By designating one direction as the reference, the other can be derived accordingly; here, the transverse direction is set as the reference. Assuming plasticity occurs only in the transverse direction and in shear, and applying the Bogetti equation for the post-yield behavior, the stress-strain relationships in shear and transverse tension can be expressed with the following relations. The assumption is based on the properties of unidirectional composites: fibers have significantly higher strength and stiffness than the matrix and exhibit limited plasticity, remaining elastic or failing in a brittle manner. Also, since fibers primarily carry the load, failure typically occurs through fiber rupture or fiber-matrix delamination, rather than plastic deformation.

$$\gamma_{12} = \frac{\tau_{12}}{G_{xy}} + \frac{Y_0\left(3\tau_{12} - \sqrt{3}R_{12}s_0\right)}{ER_{12}\left(R_{12}^p Y_0^p - \left(\sqrt{3}\tau_{12} - R_{12}s_0\right)^p\right)^{1/p}} \tag{11}$$

$$\varepsilon_{22} = \frac{\sigma_2}{E_y} + \frac{Y_0(\sigma_2 - R_2 s_0)}{ER_2\left(R_2^p Y_0^p - (\sigma_2 - R_2 s_0)^p\right)^{1/p}} \tag{12}$$

The equation introduces the parameters E, Y_0, and p, which affect the initial slope, asymptote, and curvature above the yield criterion of the reference stress-strain curve. The parameter s_0 is the starting point of the reference yield curve, i.e. the reference yield point above which the Hill model is activated. The accuracy of the curves obtained from the simulations was qualified with the Normalized Root Mean Square Deviation (NRMSD), calculated between the average stress-strain curve and the average force-displacement curves and the model curves, in the case of tensile test and 4-point-bending test results, respectively. The NRMSD is given as:

$$NRMSD\ (\%) = \frac{\sqrt{\frac{1}{n}\sum_{i=1}^{n}(y_i - \hat{y}_i)^2}}{\max_{i=1\ldots n}(\hat{y}_i)} \tag{13}$$

where y_i is the measured value, $\hat{y}_i$ is the modeled value and n is the number of data points.

3. Materials and methods

3.1. Specimen design

Samples with various fiber orientations and layer configurations were designed to measure the longitudinal, transverse, and in-plane shear characteristics. For determining the longitudinal elastic modulus (E_{11}) and Poisson's ratio (ν_{12}), unidirectional specimens with a 0° fiber orientation were used, where 0° aligns with the direction of the tensile load. To measure the transverse modulus (E_{22}), unidirectional specimens with a 90° orientation were used. The results of the 90° specimens were also used for fitting the parameters of the Hill reference nonlinear stress-strain equation. For the shear modulus (G_{12}), biaxial specimens with a symmetrical and balanced layering of ±45° orientation were applied. The biaxial specimens were also used to fit the R_{12} parameter used in Eqs. (5) and (6). Additionally, unidirectional specimens with 30°

Table 1
Layer orders of the specimens for mechanical testing.

Sample type	*Mechanical testing*	*Layer type*	Layer height (mm)	Orientation	Material
UD 0°	*Tensile test*	*Top*	0.5	[135/45]	PA
		Reinforcing	1.08	$[0]_3$	PA + CCF-1.5K
		Bottom	0.5	[45/135]	PA
UD 90°		*Top*	0.5	[135/45]	PA
		Reinforcing	1.08	$[90]_3$	PA + CCF-1.5K
		Bottom	0.5	[45/135]	PA
MD 45°/ 135°		*Top*	0.36	[135/45]	PA
		Reinforcing	1.44	[45/135/ 135/45]	PA + CCF-1.5K
		Bottom	0.36	[45/135]	PA
UD 30°		*Top*	0.5	[135/45]	PA
		Reinforcing	1.08	$[30]_3$	PA + CCF-1.5K
		Bottom	0.5	[45/135]	PA
UD 45°		*Top*	0.5	[135/45]	PA
		Reinforcing	1.08	$[45]_3$	PA + CCF-1.5K
		Bottom	0.5	[45/135]	PA
MD 0°/ 90°		*Top*	0.36	[135/45]	PA
		Reinforcing	1.44	[0/90/90/ 0]	PA + CCF-1.5K
		Bottom	0.36	[45/135]	PA
UD 0°	*4-point bending test*	*Top*	0.5	[0]	PA
		Reinforcing	0.5	[0]	PA + CCF-1.5K
		Bottom	0.5	[0]	PA
UD 0°		*Top*	0.5	[0]	PA
		Reinforcing	2	[0]	PA + CCF-1.5K
		Bottom	0.5	[0]	PA
UD 0°		*Top*	0.5	[0]	PA
		Reinforcing	3	[0]	PA + CCF-1.5K
		Bottom	0.5	[0]	PA

and 45° orientations, along with multidirectional specimens (MD) with 0°/90° orientation, were tested to assess the effects of multiaxial stress states and to validate the fitted Hill model in FE analysis. All biaxial specimens had a symmetrical and balanced layering configuration. The layer orders can be seen in Fig. 3 and the layer properties are shown in Table 1. Due to the continuous fiber laying process, contour lines are formed at the edges of the specimen. The orientation of the fibers placed along the contour lines differs from the orientation to be tested and may affect the measurement results. In order to eliminate this effect, the specimens were machined from larger plates using a precision circular table saw.

Samples for 4-point bending were prepared with UD 0°-layer order. To investigate the effect of thickness on the accuracy of the modeling method, samples were prepared with thicknesses of 1.5 mm, 3 mm, and 4 mm. The thicknesses are chosen so that the thickness of the top and bottom layers is constant, and only the thickness of the reinforced layers can be varied.

We applied solid infill with 100 % infill density for all specimens. By using 100 % infill, we aimed to eliminate the variability caused by different fill patterns, as the purpose of the measurements was to evaluate the effects of fiber orientations and to measure the intrinsic properties of the composites. We also aimed to achieve a continuous material structure with minimal porosity to ensure compatibility with the continuum mechanical model used for fitting. Following the recommendations on the materials datasheet, we set the nozzle temperature and the bed temperature to 265 °C and 60 °C, respectively. The printing speed of the first layer was 20 mm/s to ensure proper adhesion to the print bed. The printing speed of the PA layers and the polyamide/continuous carbon fiber (PA/CCF) filament was set according to the datasheets to 40 mm/s and 5 mm/s, respectively. Cooling was not applied. In the slicing software, the 'macro-layer' method was applied, where the diameter of the composite fiber determines the reference layer height and the heights of other layers are adjusted accordingly. The reference macro-layer height is an integer multiple of the unreinforced layer height.

3.2. Materials and 3D printing

Samples were manufactured with a COMPOSER A3 3D printer (Anisoprint 3D Printing Technology Limited company, Luxembourg), and the G-code files were generated with AURA 2, the dedicated software for the printer. The 3D printer (Fig. 4/a) is based on Composite Filament Co-extrusion technology (Fig. 4/b), which means it features a dual extruder print head including two hot-end blocks: one dedicated to the matrix and the other to the composite filament. The specimens were produced with Anisoprint Smooth PA matrix and continuous carbon fiber reinforcement (Anisoprint CCF-1.5K) (see Fig. 5). The Anisoprint Smooth PA material is a polyamide-12 (PA12) filled with 10 wt% short carbon fibers with a density of 1.06 g/cm^3. The continuous carbon fiber filament is impregnated with resin. Its diameter is 0.35 mm, and the fiber volume fraction is 60 %.

3.3. Mechanical properties

Tensile tests were conducted according to the ISO 527–5:2021 [28] and the ISO 14129:1997 [29] standards using a Hegewald&Perschke Inspekt table 50–1 instrument with 50 kN load cell (Kraftmesszelle) and with a crosshead speed of 2 mm/min. For strain measurement, an Epsilon 3560-BIA-025M-010-ST three-channel biaxial extensometer was used (Fig. 6/a). According to the ISO 527–5:2021 standard, we determined the σ_{11} - ε_{11} and σ_{22} - ε_{22} curves by testing 0° and 90° UD specimens. According to the ISO 14129 standard, the τ_{12} - γ_{12} curve can be given. The specimens used for validation (with fiber orientations other

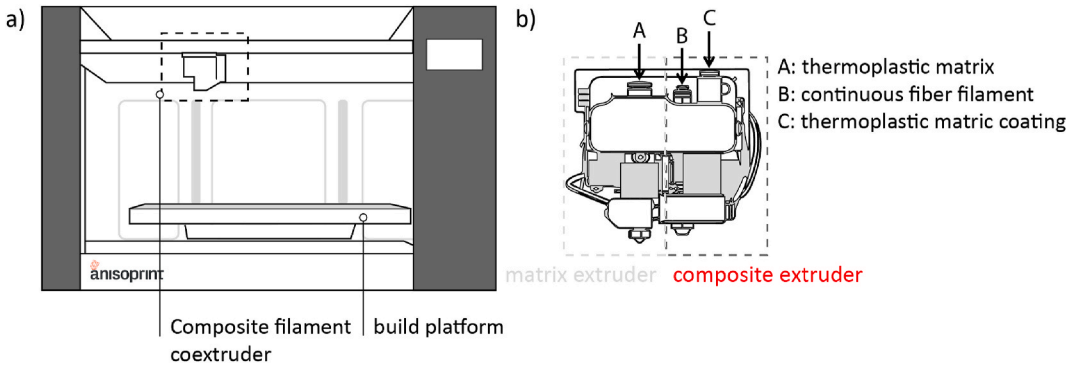

Fig. 4. Continuous fiber-reinforced 3D printing a) Anisoprint Composer A3, b) Composite Filament Co-extrusion technology [27].

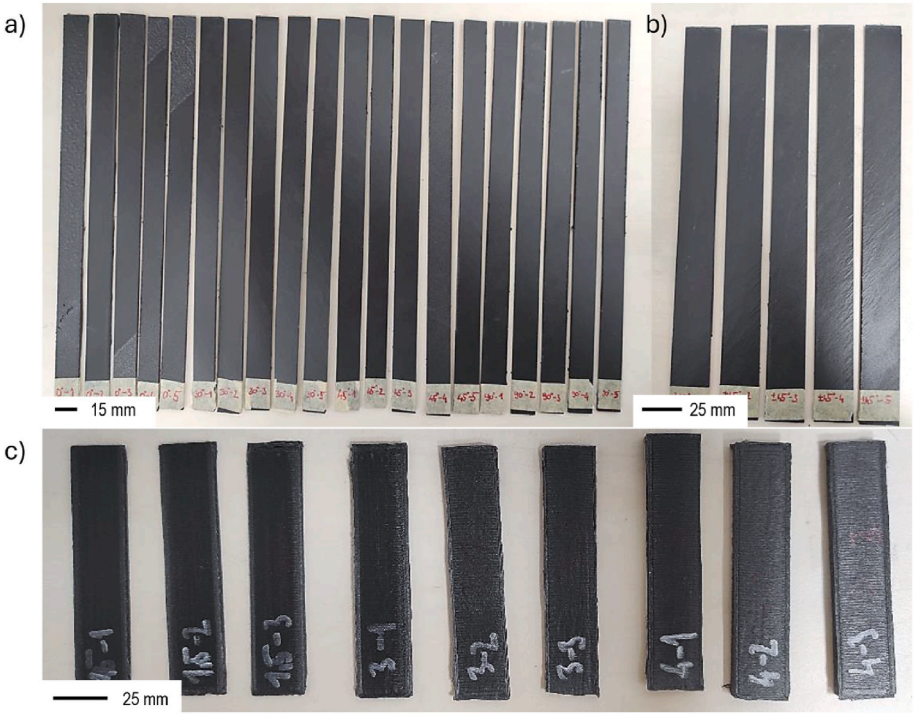

Fig. 5. 3D-printed samples a) tensile specimens according to ISO 527–5, b) tensile specimens according to ISO 14129, c) 4-point bending specimens according to ISO 14125.

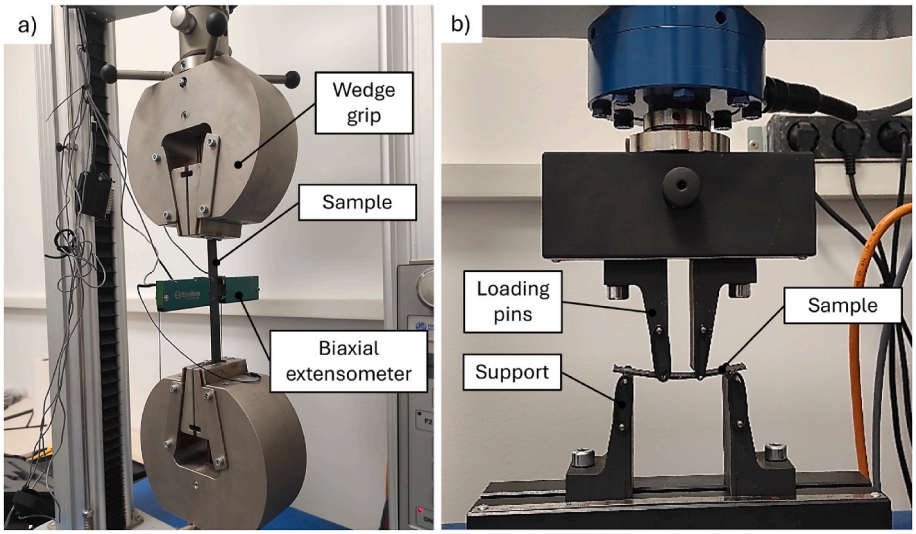

Fig. 6. Test arrangements a) tensile testing with biaxial extensometer, b) 4-point-bending test.

than 0° and 90°) were tested according to ISO 527–5. At least 5 specimens were tested for each sample type.

The composites were modeled in the FE environment as two-dimensional shell elements. The engineering constants required to describe the transversely isotropic materials were determined and are the input parameters for the CLT-based simulation. The E_{11} and Poisson's ratios are derived from the stress-strain curves determined from the longitudinal (0°) tensile test results (Eqs. (14) and (15)). The transverse modulus values (E_{22}) were determined as the chord modulus. The value of G_{12} was determined from the tensile curve of ±45° specimens as the chord modulus (Eq. (16)). Thus, the engineering constants are $E_{11} = 22.5$ GPa, $E_{22} = 903$ MPa, $G_{12} = 446$ MPa and $\nu_{12} = 0.345$.

$$E = \frac{\sigma_{0,0025} - \sigma_{0,0005}}{\varepsilon_{0,0025} - \varepsilon_{0,0005}} \tag{14}$$

$$\nu_{12} = \left| \frac{dx_y}{dx_x} \right| \tag{15}$$

$$G = \frac{\tau_{0,0025} - \tau_{0,0005}}{\gamma_{0,0025} - \gamma_{0,0005}} \tag{16}$$

4-point bending tests were conducted according to the ISO 14125:1998 [30] standard on a Hegewald&Perschke Inspekt table 50–1 instrument (Fig. 6/b). The calculated deformations were derived from the displacement of the crosshead. The crosshead speed was 2 mm/min. Samples were prepared with thicknesses of 1.5 mm, 3 mm, and 4 mm,

Table 2
Measured fiber weight and volume fractions of the composites with different fiber orientations.

Sample type	Sample mass before burnout (g)	Sample mass after burnout (g)	Pan mass (g)	Fiber weight fraction, V_f (%)	Fiber volume fraction, v_f (%)
UD 0°	46.3	40.8	39.1	23.8	11.7
UD 30°	45.7	40.0	38.2	24.2	12.4
UD 45°	34.1	28.9	27.5	20.9	9.5
UD 90°	46.3	40.6	38.8	23.8	12.1
MD [0/90]	38.7	32.2	30.2	23.3	13.6
MD [45/135]	51.3	42.5	39.2	27.6	13.6

for which the support spans were 24.75 mm, 49.5 mm and 66 mm, respectively. At least 5 specimens were tested for each sample type.

3.4. Microstructure

Scanning Electron Microscope (SEM) images of the fracture surfaces were taken with a JSM 6380LA scanning electron microscope from Jeol Ltd. (Japan). The samples were sputtered with gold to avoid static charging.

X-ray tomography measurements were performed with Nikon XT H 225 ST (Nikon, Japan) equipment to obtain information on the inhomogeneity and porosity of the 3D-printed specimens. The resolution was 3–5 μm. The instrument consists of a single reflection X-ray tube, the applied accelerating voltage was 225 kV, the cathode current was 65 mA and the data acquisition time was 0.5 s. For the measurements, the samples were placed on a five-axis sample holder and rotated once along the vertical axis. During the rotation, the device captured 1250 images. To analyze the porosity, we used the VG-EasyPore porosity analysis

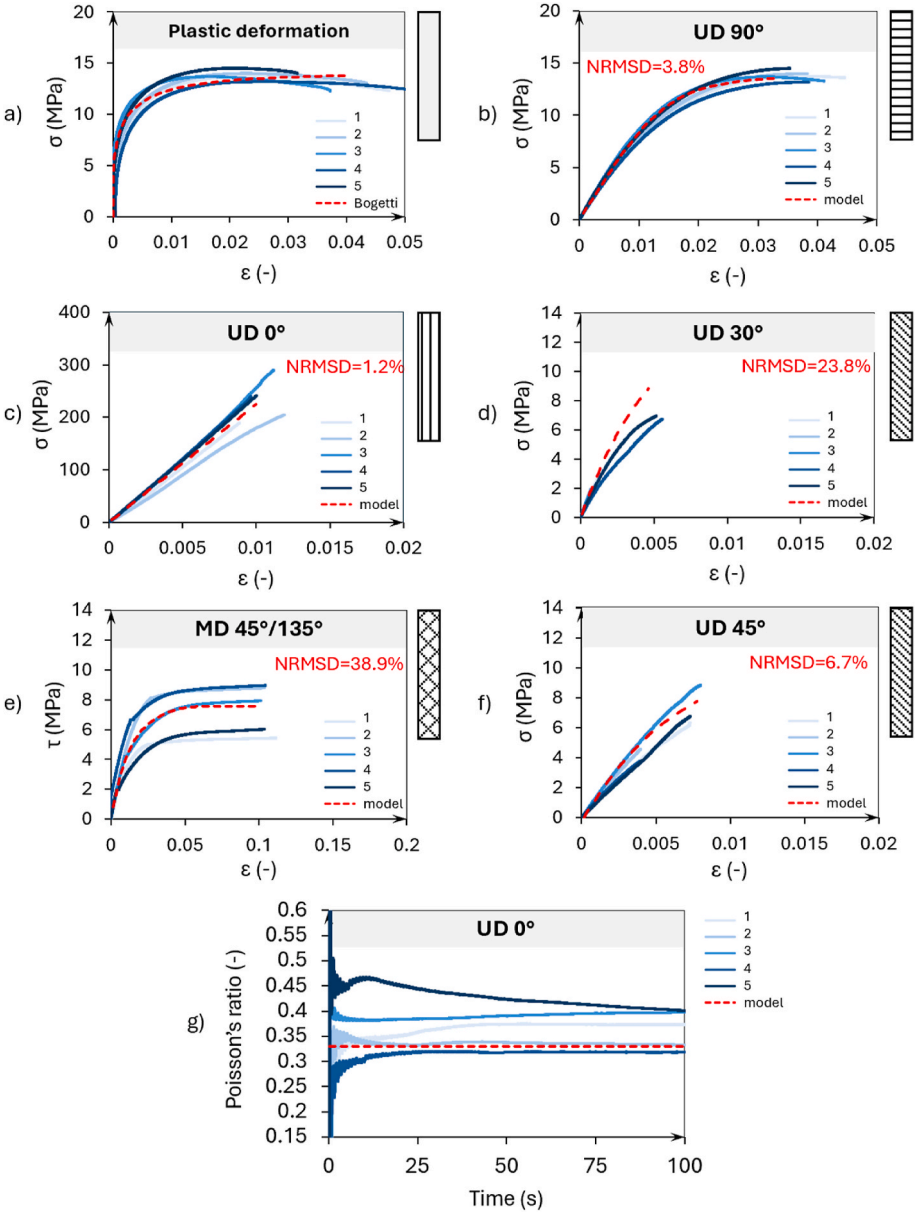

Fig. 7. a) Bogetti curve fitted against the transverse tensile results where plastic strain is plotted against stress; total strain against stress shown in the case of b) UD 90°, c) UD 0°, d) UD 30°, e) MD 45°/135°, f) UD 45° specimen types; g) fitting of the Poisson's ratio to the UD 0° test results.

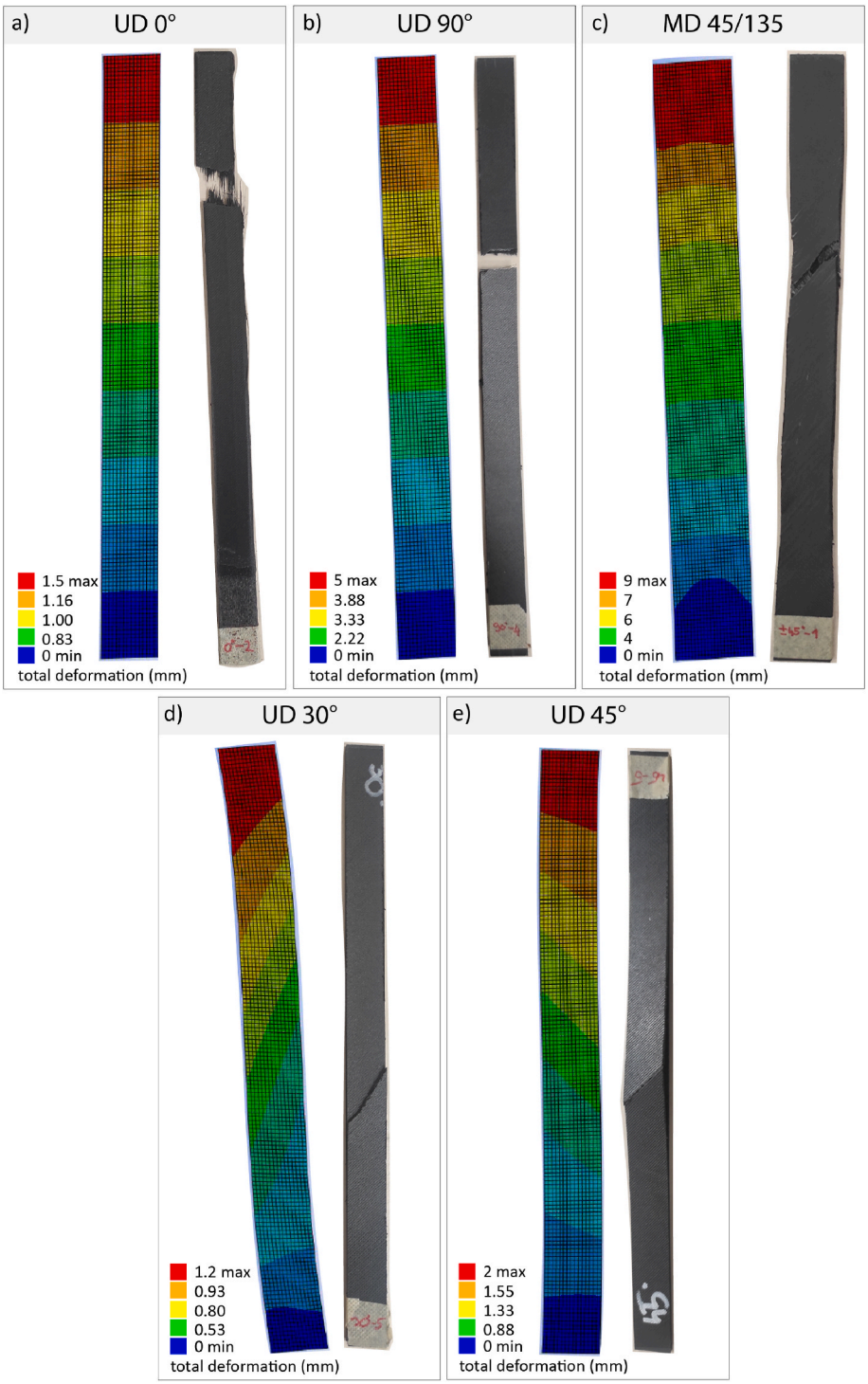

Fig. 8. Total deformation obtained via FEM and photographs of the samples after failure in the case of a) UD 0°, b) UD 90°, c) MD 45°/135°, d) UD 30°, e) UD 45° specimen types.

algorithm.

To determine the fiber volume fraction, samples were placed in a Denkal 6B furnace at 500 °C for 4 h. The test method was defined according to the ASTM D 3171-99 standard [31]. The mass of the samples before burning and the mass of the remaining fibers after the decomposition of the matrix material were also measured. The fiber volume content (v_f) was obtained with Eq. (17).

$$v_f = \frac{(m_{fibers} - m_{vessel})}{b \cdot h \cdot L \cdot \rho_f} \cdot 100\ (\%) \tag{17}$$

where m_{fibers} (g) is the mass of fibers remaining after burning including the vessel, m_{vessel} (g) is the mass of the sample holder, b, h, and l (mm) are the width, thickness, and length, respectively and $\rho_f = 1.8$ (g/cm^3) is the density of the carbon fibers.

Table 2 presents the measured fiber content for samples with varying orientations.

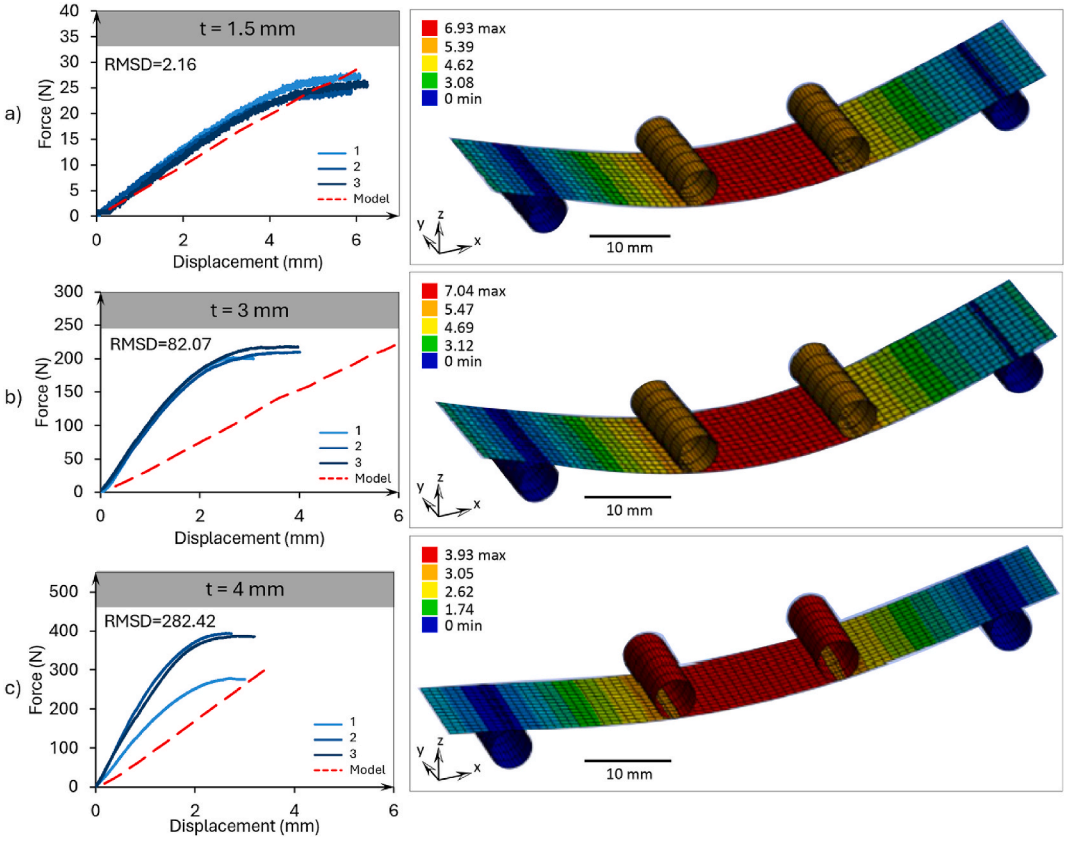

Fig. 9. Measured and modeled force-crosshead displacement curves in the case of specimen thickness of a) 1.5 mm, b) 3 mm, and c) 4 mm.

4. Results and discussion

4.1. Tensile load simulations

In polymer composites with continuous fiber reinforcement, nonlinear behavior during loading can result from both the tough matrix and the varying orientations of the fibers. For fibers aligned in the 0° orientation, an almost completely linear response to tensile loading is observed. However, for fibers in other orientations, the stress-strain curves display degressive characteristics. This phenomenon may occur because the reinforcing effect of the fibers is most pronounced when the applied stress aligns with the fiber direction (0° orientation). As the fiber orientation deviates, the matrix material's nonlinear viscous behavior becomes increasingly dominant.

To address the nonlinearity, elastic constants and constants of the Bogetti equation were fitted to the tensile test results of the 0°, 90°, and ± 45° specimens. Then, the model was validated with the off-axis tensile tests. The bottom and top layers were treated as the matrix of the entire composite, allowing the specimen to be considered as a homogeneous layer. Using the Hill model, the principal stress-strain curves are rescaled using the R-ratios (Hill parameters), so that the behavior of other orientations can be modeled with a principal reference curve and corresponding R-values. The initial dataset was the tensile curves obtained with 90° UD specimens. First, the elastic components were extracted from the transverse specimen tensile curves, and the Bogetti equation was fitted to the resulting stress-plastic deformation curve (Fig. 7/a). The fitted parameters were E = 700 MPa, Y0 = 17 MPa, and p = 1.8. This curve served as the reference for the hardening rule, which requires a series of stress-plastic deformation data points. Then, we determined the R parameters, with the approximation that the plastic deformation is initiated immediately upon application of the load. Thus, $s_0 \rightarrow 0$. The R parameters acquired with Eq. (18) were $R_1 = 10^6$, $R_2 = 1$, and $R_{12} = 1.81$. The value of R_1 is set to a sufficiently large number to ensure that only linear behavior is assumed for 0°. R_2 is set to 1 because the 90° curves are used as a reference.

$$\gamma_{12} = \frac{\tau_{12}}{G_{12}} + \frac{Y_0 \cdot 3\tau_{12}}{ER_{12}\left(R_{12}^p Y_0^p - \left(\sqrt{3}\,\tau_{12}\right)^p\right)^{1/p}} \tag{18}$$

Fig. 7/b-f shows the model curves obtained with the Finite Element Modeling (FEM) method and the experimental tensile curves. The Poisson's ratio was measured on UD 0° specimens using a biaxial extensometer. The results are shown in Fig. 7/g. The fitting resulted in a Poisson's ratio of 0.3355. The NRMSD values are also shown in Fig. 7. The highest deviation was obtained in the case of the MD 45°/135° samples (38.9 %). It can be seen that the curves obtained by the modeling method are generally a good approximation of the measurement results. The estimates follow well the nonlinear characteristics of the different UD and MD samples. Fig. 8 shows the total deformation obtained via FEM and photographs of the samples after failure. The photographs show that the crack propagation follows the fiber orientation. This is due to the weaker contact between the fiber bundles, and the micrographs also revealed the presence of voids between the bundles.

In general, these 3D-printed composites have lower mechanical properties, due to the lower fiber content achieved by 3D printing and the presence of voids and other printing defects [32]. Despite this, the reference Hill curve describing the transverse behavior can be well rescaled to the shear curve, as the average fit is good in the case of the 45°/135° specimens despite the significant scatter. The micro-tomography results show that the 45°/135° samples have a high void content (18.76 %), which may explain the scatter. In the validation tests, the simulations generally reproduced the measurements with high accuracy. For the 30° UD case, the model slightly overestimates the stiffness, and for the off-axis cases, the model curve appears to show a

Table 3
Measured porosity of the unreinforced PA, and the composites with different fiber orientations. Measurements were taken with microtomography.

Sample type	Porosity (%)
Unreinforced PA	5.47
UD 0°	6.89
UD 45°	11.17
MD [0/90]	19.97
MD [45/135]	18.76

slightly higher nonlinearity. Similar mechanical properties are reported in the literature for 3D-printed carbon fiber reinforced composites with PA matrix. Chacón et al. [33] reported a tensile strength of 239.8 MPa in case of UD composites with 15 % fiber volume content. Azarov et al. [34] prepared UD composites with Anisoprint 3D printing equipment as in the current study. The authors measured a tensile strength of 330 MPa at 18 % fiber volume content.

4.2. Application boundaries

In the tensile test simulations, the composites were modeled as two-dimensional shells, with all out-of-plane effects, including interlayer stresses, neglected. This approximation is sufficiently accurate only for thin, plate-like components. As validation, four-point bending tests were conducted. The flexural specimens were prepared with varying thicknesses, oriented at 0°, and with the same fiber content as the tensile specimens. The composite specimen's layering was configured in the Ansys Composites PrepPost (ACP) module in ANSYS Workbench 2021 R2, while the grips and loads were specified in the Static Structural module. Frictionless contacts with a Normal Lagrange setting were applied at the support and thrust roller interfaces. In the case of constant support distance, as the thickness increases, the effect of inter-layer stiffness intensifies. This results in an overestimation of deflection in the simulations.

Results are shown in Fig. 9. The measured force-crosshead displacement curves show an initial linear phase, followed by a plateau. The initial phase results from the tensile response of fibers oriented at 0°. At the initial phase, the model approximates the curve from below. This is because the interlaminar stiffness was zero, however, at this phase, it would contribute to the bending stiffness significantly. The plateau may be attributed to the nonlinear behavior on the compressed side, or fiber pullout due to weak adhesion between the fiber and matrix. The plateau can also be caused by the fact that at large deflections the test specimen's test cross-section rotates like a rigid body, which does not mean actual deformation, so the force increment that produces this is no longer proportional to the value measured in the previous linear section. When fiber-matrix separation occurs, the matrix behavior becomes dominant at larger deflections. Unlike the measured results, the simulation curves remain linear, as the model does not account for differences in tensile and compressive characteristics. For standard plate-like specimens, the simulation curve aligns closely with the measured values. However, as the thickness increases, the simulation considerably underestimates the force values, due to the two-dimensional model's omission of interlaminar stresses. In thicker specimens, these interlaminar effects become more pronounced, causing measured values to exceed those predicted by the simulation.

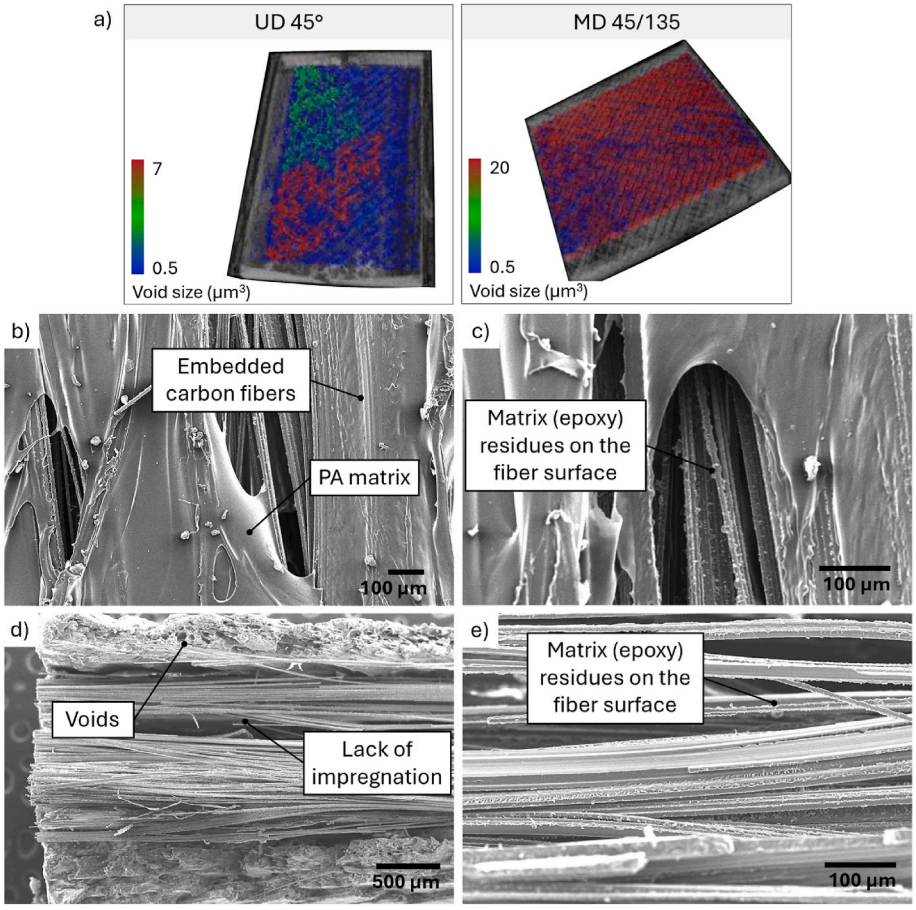

Fig. 10. a) Microtomography images taken from UD 45° and MD 45°/135° type samples; SEM micrographs taken from MD 45°/135° type sample with b) 100x and c) 200 magnification, and UD 90° type sample with d) 35x and e) 200× magnification.

4.3. Microstructure

To evaluate the mechanical test and to construct the material model, it is essential to understand the specific defects associated with the production technology and their frequency in the test specimens. The actual fiber content and porosity were determined, and the quality of adhesion between fibers and matrix was also assessed. Microtomography measurements were conducted to determine the porosity of unreinforced PA and fiber-reinforced PA specimens. The pure PA specimen exhibited a porosity of 5.47 %, indicating a high-quality print. In contrast, unidirectionally and bidirectionally reinforced specimens showed significantly higher porosity within the reinforced layers. Table 3 summarizes the measured porosity of the neat PA, and the UD 0°, UD 45°, MD 0°/90°, and the MD 45°/135° type specimens. The highest porosity was measured in the case of the MD 0°/90° type (~20 %). The lower porosity values are in line with the literature [35,36]. Liu et al. [35] also observed that lower porosity can be achieved by applying slower printing speed.

Fig. 10 shows microtomography images of a unidirectional and a bidirectional sample. The bidirectionally reinforced specimens exhibited even larger gaps, which was reflected in their increased porosity values. It was observed that larger air gaps formed along the fiber paths, revealing a drawn-out infill pattern in both the pure PA and composite specimens. Scanning electron microscopy was used to capture images of the tensile test specimens after failure. Fig. 10/b and c were taken from MD 45°/135° type specimens. The micrographs suggest that the fibers are well embedded in the PA matrix, and Fig. 10/c also reveals fragments of matrix material on the fiber surfaces. The residues on the surface indicate good fiber-matrix bonding. Fig. 10/d and e were taken from a UD 90° type specimen. When the fibers are deposited in several layers in the same orientation, it can be seen that less matrix material is placed between them during production, resulting in voids. This was also shown in the microtomography images. Lack of impregnation can induce premature failure due to inadequate load transfer between the fiber and the matrix.

5. Conclusion

We present a layer-level constitutive material model to describe the nonlinear mechanical response of continuous fiber-reinforced 3D-printed composites. Unidirectional and multidirectional samples were prepared for tensile testing using Composite Filament Co-extrusion technology with polyamide matrix and carbon fiber reinforcement. Thermoplastic composites exhibit significant nonlinearity, as permanent deformation occurs under lower stress levels and the thermoplastic matrix exhibits viscoelastic behavior. We determined the engineering constants required to describe the transversely isotropic materials, then we applied the Bogetti relationship based on the explicit Ramberg-Osgood equation to describe the curve above the yield criterion. The principal stress-strain curves were rescaled using the Hill model and it was shown that the Hill curve describing the transverse behavior can be rescaled well to the shear curve. Application boundaries were evaluated with 4-point bending simulations. We show that for standard plate-like specimens (1.5 mm thickness), the simulation curve closely fits the measured values. However, as the thickness increases (above 3 mm), the simulation underestimates the force values because the two-dimensional model does not take into account differences in tensile and compressive properties and inter-layer stresses. Our method extends the current capabilities for constitutive modeling of 3D-printed thermoplastic composites. As the use of 3D-printed continuous fiber reinforced structures becomes more widespread in industries requiring lightweight yet strong materials, accurate characterization of nonlinear behavior is important for predicting the mechanical properties and for safe application.

CRediT authorship contribution statement

Csenge Tóth: Writing – original draft, Visualization, Supervision. **Blanka Ilinyi:** Writing – original draft, Validation, Investigation, Formal analysis. **László Kovács:** Writing – review & editing, Supervision, Project administration, Methodology, Funding acquisition, Conceptualization.

Declaration of competing interest

The authors declare that they have no known competing financial interests or personal relationships that could have appeared to influence the work reported in this paper.

Acknowledgements

Project no. TKP-6-6/PALY-2021 has been implemented with the support provided by the Ministry of Culture and Innovation of Hungary from the National Research, Development and Innovation Fund, financed under the TKP2021-NVA funding scheme. Csenge Tóth is thankful for the support of the EKÖP-24-4-I-BME-198 University Research Fellowship Programme of the Ministry for Culture and Innovation from the source of the National Research, Development and Innovation Fund. The research reported in this paper was supported by the National Research, Development and Innovation Office (NRDI, Hungary) through grants K146236. The project is also funded by the National Research, Development and Innovation (NKFIH) Fund, Project title: Precision characterization of nonlinear mechanical behavior of reinforced and unreinforced polymeric materials for engineering simulations"; The application ID number: 2020–1.1.2-PIACI-KFI-2021-00314. The developers are grateful for the support.

Data availability

Data will be made available on request.

References

[1] P. Cheng, Y. Peng, S. Li, Y. Rao, A. Le Duigou, K. Wang, S. Ahzi, 3D printed continuous fiber reinforced composite lightweight structures: a review and outlook, Compos. B Eng. 250 (2023), https://doi.org/10.1016/j.compositesb.2022.110450.

[2] Y. Huang, X. Tian, L. Wu, A.A. Zia, T. Liu, D. Li, Progressive concurrent topological optimization with variable fiber orientation and content for 3D printed continuous fiber reinforced polymer composites, Compos. B Eng. 255 (2023) 110602, https://doi.org/10.1016/j.compositesb.2023.110602.

[3] C. Quan, B. Han, Z. Hou, Q. Zhang, X. Tian, T.J. Lu, 3d printed continuous fiber reinforced composite auxetic honeycomb structures, Compos. B Eng. 187 (2020) 107858, https://doi.org/10.1016/j.compositesb.2020.107858.

[4] C. Zeng, L. Liu, W. Bian, J. Leng, Y. Liu, Bending performance and failure behavior of 3D printed continuous fiber reinforced composite corrugated sandwich structures with shape memory capability, Compos. Struct. 262 (2021), https://doi.org/10.1016/j.compstruct.2021.113626.

[5] L. Liu, Y. Miao, Q. Deng, X. Hu, Y. Zhang, R. Wang, Y. Wang, M. Su, Y.-W. Mai, Rate-dependent mechanical and self-monitoring behaviors of 3D printed continuous carbon fiber composites, Compos. Sci. Technol. 259 (2025) 110914, https://doi.org/10.1016/j.compscitech.2024.110914.

[6] W. Ye, H. Dou, Y. Cheng, D. Zhang, S. Lin, Mechanical and self-sensing properties of 3D printed continuous carbon fiber reinforced composites, Polym. Compos. 43 (2022) 7428–7437, https://doi.org/10.1002/pc.26825.

[7] X. Zhang, X. Zheng, Y. Han, Y. Tian, D. Zhang, L. Yan, Failure mechanisms and process defects of 3D-printed continuous carbon fiber-reinforced composite circular honeycomb structures with different stacking directions, Aero. Sci. Technol. 148 (2024) 109075, https://doi.org/10.1016/j.ast.2024.109075.

[8] K.-J. Lee, M.-S. Jeon, J.-R. Lee, Evaluation of manufacturing defects in 3D printed carbon fiber reinforced cylindrical composite structure based on laser ultrasonic testing, NDT E Int. 135 (2023) 102802, https://doi.org/10.1016/j.ndteint.2023.102802.

[9] G.Z. Marton, G. Szebényi, Influencing the damage process and failure behaviour of polymer composites – a short review, Express Polym. Lett. 19 (2025) 140–160, https://doi.org/10.3144/expresspolymlett.2025.11.

[10] E.J. Barbero, Introduction to Composite Materials Design, third ed., CRC Press., Boca Raton, 2017.

[11] C. Savandaiah, A. Kapshammer, B. Plank, V. Stolcer, C. Marschik, Z. Major, Thermo-mechanical characterisation of polycarbonate-based sheet moulded composites fabricated from off-cut waste unidirectional tapes, Express Polym. Lett. 18 (2024) 883–900, https://doi.org/10.3144/expresspolymlett.2024.66.
[12] J.L. Chen, C.T. Sun, Modeling of orthotropic elastic-plastic properties of ARALL laminates, Compos. Sci. Technol. 36 (1989) 321–337, https://doi.org/10.1016/0266-3538(89)90045-6.
[13] D. Kenaga, J.F. Doyle, C.T. Sun, Characterization of boron/aluminum composite in the nonlinear range as an orthotropic elastic-plastic material, J. Compos. Mater 21 (1987), https://doi.org/10.1177/002199838702100603.
[14] C.T. Sun, J.L. Chen, A micromechanical model for plastic behavior of fibrous composites, Compos. Sci. Technol. 40 (1991) 115–129, https://doi.org/10.1016/0266-3538(91)90092-4.
[15] R. Von Mises, Mechanik der festen Körper im plastisch-deformablen Zustand. Nachrichten von der Gesellschaft der Wissenschaften zu Göttingen, Mathematisch-Physikalische Klasse 1 (1913) 582–592.
[16] I.M. Alarifi, PETG/carbon fiber composites with different structures produced by 3D printing, Polym. Test. 120 (2023) 107949, https://doi.org/10.1016/j.polymertesting.2023.107949.
[17] Z. Hou, X. Tian, Z. Zheng, J. Zhang, L. Zhe, D. Li, A. V Malakhov, A.N. Polilov, A constitutive model for 3D printed continuous fiber reinforced composite structures with variable fiber content, Compos. B Eng. 189 (2020) 107893, https://doi.org/10.1016/j.compositesb.2020.107893.
[18] A. Avanzini, D. Battini, L. Giorleo, Finite element modelling of 3D printed continuous carbon fiber composites: embedded elements technique and experimental validation, Compos. Struct. 292 (2022) 115631, https://doi.org/10.1016/j.compstruct.2022.115631.
[19] A.M. Seifans, S. Ayyagari, M. Al-Haik, Elastic/viscoplastic characterization of additively manufactured composite based on continuous carbon fibers, Aero. Sci. Technol. 111 (2021) 106562, https://doi.org/10.1016/j.ast.2021.106562.
[20] E. Polyzos, D. Van Hemelrijck, L. Pyl, Numerical modelling of the elastic properties of 3D-printed specimens of thermoplastic matrix reinforced with continuous fibres, Compos. B Eng. 211 (2021) 108671, https://doi.org/10.1016/J.COMPOSITESB.2021.108671.
[21] J. Gao, B. Li, H. Bu, X. Li, X. Zhan, Effect of infill density and reinforced perimeters on tensile properties and fracture mechanism of 3D printing carbon fiber–reinforced composite, Int. J. Adv. Des. Manuf. Technol. 128 (2023) 267–281, https://doi.org/10.1007/s00170-023-11871-7.
[22] P. Máté, A. Szekrényes, The effect of the layup on the stability of composite cylindrical shells, Period. Polytech. - Mech. Eng. 68 (2024) 291–303, https://doi.org/10.3311/PPme.23424.
[23] S.-Q. Yang, J. Yang, P. Xu, Analysis on pre-peak deformation and energy dissipation characteristics of sandstone under triaxial cyclic loading, Geomech. Geophys.Geo-Energy Geo-Res. 6 (2020) 24, https://doi.org/10.1007/s40948-020-00146-0.
[24] L. Cheng, H. Xu, S. Li, X. Liu, Z. Liu, Characterization of crack evolution and hardening-softening in rock elastoplastic constitutive models, Comput. Geotech. 176 (2024) 106711, https://doi.org/10.1016/j.compgeo.2024.106711.
[25] T.A. Bogetti, J.W. Gillespie, M.A. Lamontia, The influence of ply waviness with nonlinear shear on the stiffness and strength reduction of composite laminates, J. Thermoplast. Compos. Mater. 7 (1994) 76–90, https://doi.org/10.1177/089270579400700201.
[26] Rodney Hill, The Mathematical Theory of Plasticity, Clarendon Press, Oxford, 1998.
[27] A. Adumitroaie, F. Antonov, A. Khaziev, A. Azarov, M. Golubev, V.V. Vasiliev, Novel continuous fiber bi-matrix composite 3-D printing technology, Materials 12 (2019), https://doi.org/10.3390/ma12183011.
[28] International Organization for Standardization, Plastics — Determination of Tensile Properties, ISO, 2021, 527-5.
[29] International Organization for Standardization, Fibre-reinforced plastic composites — determination of the in-plane shear stress/shear strain response, including the in-plane shear modulus and strength, by the plus or minus 45 degree tension test method, ISO (1997) 14129.
[30] International Organization for Standardization, Fibre-reinforced Plastic Composites — Determination of Flexural Properties, 1998. ISO 14125.
[31] ASTM International, Standard Test Methods for Constituent Content of Composite Materials, D3vols. 171–99, ASTM, 1999.
[32] E.C. Botelho, Ł. Figiel, M.C. Rezende, B. Lauke, Mechanical behavior of carbon fiber reinforced polyamide composites, Compos. Sci. Technol. 63 (2003) 1843–1855, https://doi.org/10.1016/S0266-3538(03)00119-2.
[33] J.M. Chacón, M.A. Caminero, P.J. Núñez, E. García-Plaza, I. García-Moreno, J. M. Reverte, Additive manufacturing of continuous fibre reinforced thermoplastic composites using fused deposition modelling: effect of process parameters on mechanical properties, Compos. Sci. Technol. 181 (2019), https://doi.org/10.1016/j.compscitech.2019.107688.
[34] A. V Azarov, F.K. Antonov, M. V Golubev, A.R. Khaziev, S.A. Ushanov, Composite 3D printing for the small size unmanned aerial vehicle structure, Compos. B Eng. 169 (2019) 157–163, https://doi.org/10.1016/j.compositesb.2019.03.073.
[35] F. Liu, E. Ferraris, J. Ivens, Mechanical investigation and microstructure performance of a two-matrix continuous carbon fibre composite fabricated by 3D printing, J. Manuf. Process. 79 (2022) 383–393, https://doi.org/10.1016/j.jmapro.2022.04.050.
[36] K. Dvorak, L. Zarybnicka, R. Ševčík, M. Vopalensky, I. Adamkova, 3D composite printing: study of carbon fiber incorporation to different construction thermoplastic matrices in regard to dilatation characteristics, Rapid Prototyp. J. 30 (2024) 1149–1160, https://doi.org/10.1108/RPJ-12-2023-0450.